Positive influence of minute Pt addition on the activity of Ni supported on defective graphene for hydrogenation/dehydrogenation of N-ethylcarbazole as liquid organic carrier

Alberto Garcia-Baldovi [a], Lu Peng [a], Amarajothi Dhakshinamoorthy [a], Abdullah M. Asiri [b], Ana Primo [a], Hermenegildo Garcia [a, b, *]

[a] *Instituto Universitario de Tecnología Química, Consejo Superior de Investigaciones Científicas-Universitat Politecnica de Valencia, Universitat Politecnica de Valencia, Av. De los Naranjos s/n, 46022, Valencia, Spain*
[b] *Center of Excellence in Advanced Materials Research, King Abdullaziz University, Jeddah, Saudi Arabia*

A B S T R A C T

Ni nanoparticles ($\approx$ 8 nm) have been prepared at about 15 wt% loading strongly grafted on N-doped graphitic carbon matrix [Ni@(N)C] by pyrolysis of Ni(OAc)$_2$ adsorbed on chitosan. Ni@(N)C was used as catalyst for H$_2$ storage/release on N-ethylcarbazole (EC). Ni@(N)C exhibits higher H$_2$ storage capacity than analogous Ni nanoparticles (NPs) supported on silica. The addition of minute amounts (18 ppm) of Pt increases significantly the H$_2$ storage/release activity of Ni@(N)C due to effect of Pt promoting H spill over the Ni NPs. There is no linear correlation between Pt concentration and hydrogenation/dehydrogenation activity of Ni@(N)C, the lowest Pt loading (18 ppm) resulting in the most efficient Pt/Ni@(N)C for hydrogenation-dehydrogenation of EC. This fact was attributed to the presence of small Pt clusters or single atoms, while higher concentration would correspond to a less-efficient larger cluster regime. The most efficient Pt/Ni@(N)C-18 catalyst was used for four consecutive hydrogenation/dehydrogenation cycles, exhibiting some fatigue in the H$_2$ storage/release of the same EC batch that was attributed to the increase in the product mixture complexity upon cycling, with the formation of some intermediates that undergo more difficult hydrogenation/dehydrogenation reaction as well as partial catalyst deactivation. After four cycles, (Pt)Ni@(N)C exhibits in the fifth use a H$_2$ storage capacity of 5.2 wt%, somewhat lower than the 5.8 wt% H$_2$ capacity of the fresh sample, while no changes in the XRD, TEM and XPS characterization of the five-times used catalyst compared to the fresh material is observed.

1. Introduction

In the context of implementing the hydrogen economy and more specifically the use hydrogen as energy vector for transportation, there is a large interest in finding suitable liquid organic compounds that can store significant percentages of hydrogen and in developing catalytic processes to release hydrogen from them upon on-board demand [1–7]. Among the most studied liquid organic hydrogen carriers (LOHC), one that has been considered as an advantageous LOHC candidate is 9-ethylcarbazole (EC) [8–12]. This condensed nitrogenated heterocyclic compound can load up to six hydrogen molecules with a theoretical hydrogen storage percentage about 5.8 wt%. Considering the nature of the reactions involved, the process requires of efficient and cost-effective

hydrogenation/dehydrogenation catalysts (Scheme 1).

Among the reported catalysts, those that have shown better performance include noble and semi noble metals (Pt, Rh [13], Pd [13–17] and Ru [8,15,18]). To have some possibility of large-scale implementation, the use of abundant first-row transition metals as catalysts, particularly Ni, is required [8,15]. Precedents in the literature have shown, however, that Ni NPs supported on metal oxides working at temperatures below 200 °C require high metal-to-substrate ratios, even above 15 wt%, to achieve high percentage of hydrogen storage capacity close to the theoretical value, making the process of low practical use [13,19]. Therefore, there is still plenty of room to develop more efficient heterogeneous catalysts to bring EC closer to any potential use as LOHC. One valid strategy to enhance the unsatisfactory catalytic activity of Ni

is by alloying and/or addition of promoters. In this regard, bimetallic Ni—Ru catalysts have been studied trying to combine the higher activity of Ru as EC hydrogenation catalyst with the advantage of Ni in terms of abundance and economic attractiveness [20,21]. Promotion of the poor Ni activity by YH_3 has also been reported [19].

In a seminal work, Corma and co-workers showed that the catalytic activity of Au for the selective hydrogenation of aromatic nitro compounds can be increased significantly upon addition of only minute amounts of Pt, without compromising the high product selectivity characteristic of Au that is absent in unselective Pt catalysts [22,23]. In this study, it was proposed that Pt, being much more efficient than gold to activate H_2, spills over hydrogen atoms on Au NPs forming gold hydrides that subsequently catalyse the nitro group reduction with their characteristic high Au chemoselectivity towards nitro group. In this way, the slowest step on Au catalysts being H—H bond breaking due to its high activation energy on Au becomes significantly accelerated by the presence of Pt in minute amounts, increasing the overall reaction rate for hydrogenation without compromising the selectivity derived from the Au—H hydride [23,24].

Inspired by this work, herein it will be shown that the catalytic activity for EC hydrogenation/dehydrogenation by Ni can be promoted by deposition of Pt in very minute amounts (ppm). In this way, the catalytic system based on Ni with 0.0018 wt% Pt (18 ppm) on N-doped graphitic carbon appears to be among the most effective solid catalyst for EC, while still essentially being based on earth abundant materials. N-doped graphitic carbons are suitable supports for metal NPs as catalysts, since they can stabilize their size by establishing strong metal-support interactions and can modulate the electron density on the metal NPs by charge transfer [25–27]. In a recent related study, the promotional effect of Rh at 10000 ppm on the catalytic activity of Ni NPs on γ-Al_2O_3 has also been reported [13]. However, in this precedent, this promotional effect of Rh has been attributed mainly to the effect on Rh on the average Ni particle size that decreases from 13.6 to 4.6 nm and to the electron transfer from Rh to Ni. In contrast, in the present study, a series of samples with much lower Pt amounts of 18 and 54 ppm were employed, while the Ni average particle size was essentially constant at about 8 nm. Therefore, the influence of Pt on Ni cannot be attributed to larger Ni atom dispersion on the catalyst.

2. Experimental section

2.1. Materials

Commercially available reagents were purchased from Aldrich and used without further purification.

2.2. Synthesis of Pt/Ni@(N)G

Samples Pt/Ni@(N)G were prepared by impregnation of chitosan beads in ethanol solution with nickel salts. Briefly, 1000 mg chitosan, a certain amount of $H_2PtCl_6 \cdot (H_2O)_6$ and 625 μL acetic acid were added into 50 mL milli-Q water. The exact Pt amounts are indicated in Table S1 in the supporting information. After chitosan powder dissolved completely, the solution was introduced dropwise, with a syringe (0.8 mm diameter needle), in an aqueous solution of potassium hydroxide (2 M). The gel microspheres were formed and immersed in KOH solution

for 2 h, then profusely washed with distilled water until the washing water had pH = 7. Then, the resulting hydrogel microspheres were washed by a series of ethanol/water baths with an increasing concentration of ethanol (10, 30, 50, 70, 90 and 100 vol%, respectively) for 15 min in each. Afterwards, the alcogel microspheres were immersed in 100 mL ethanol solution with different concentration of nickel salts for 2 days under slow stirring, then washed with anhydrous ethanol and exchanged by supercritical CO_2. The exact Ni amounts are indicated in Table S1 in the supporting information. The resulting aerogel microspheres were pyrolyzed under Ar flow (200 mL/min), increasing the temperature at a rate of 2 °C min^{-1} up to 200 °C for 2 h and then to 900 °C for 2 h. Samples Pt/Ni@(N)G-18 and Pt/Ni@(N)G-56 were prepared by the precipitation of sodium hydroxide instead of potassium hydroxide. Samples from Pt/Ni@(N)G-0 to Pt/Ni@(N)G-450 were impregnated in ethanol solution of $Ni(OAc)_2$, while sample Pt/Ni@(N) G-180000 was impregnated in ethanol solution of $NiCl_2$.

2.3. Sample characterization

X-ray diffraction (XRD) patterns were obtained in a Philips XPert diffractometer (40 kV and 45 mA) equipped with a graphite monochromator employing Ni-filtered Cu Kα radiation (1.541178 Å). Raman spectra were collected with a Horiba Jobin Yvon-Labram HR UV–visible-NIR (200–1600 nm). Raman microscope spectrometer using a 514 nm laser. The chemical composition of the samples was determined by combustion chemical analysis by using a CHNS FISONS elemental analyser. Field emission scanning electron microscopy (HRFESEM) images were acquired by using Zeiss (ULTRA 55). HRTEM images were recorded in a JEOL JEM 2100F under an accelerating voltage of 200 kV. Samples were prepared by applying one drop of the suspended material in ethanol onto a carbon-coated copper TEM grid and allowing them to dry at room temperature. H_2 pulsed sorption measurements were carried out in a Micromeritics AutoChem II 2920 station. Before H_2 adsorption, the fresh samples were heated at 250 °C at a rate of 10 °C min^{-1} in a 30 mL × min^{-1} He flow to desorb moisture and other possible adsorbates on the surface. Subsequently, the samples were cooled down to room temperature keeping constant the He flow. Afterwards, the activated materials were exposed to pulses of 5 vol% H_2 in He until the peak area corresponding to H_2 gas becomes constant and no further H_2 uptake takes place. Subsequently, H_2 thermal desorption was carried out heating the sample at a constant rate of 10 °C min^{-1} in He flow up to 450 °C.

2.4. Catalytic measurements

The hydrogenation reaction was carried out in a stainless-steel reactor, capable of holding high pressure at high temperature. Previously before the catalytic reaction 30 mg of catalyst were activated at 200 °C under hydrogen atmosphere. Immediately afterwards, 50 mg of EC and 6 mL of cyclohexane were added to the activated catalyst. The reactor was closed and purged with nitrogen gas to remove atmospheric air. Then, the reactor was sealed and filled with 40 bar of hydrogen. This heterogeneous mixture was vigorously stirred at 200 °C during 5 h. On the other hand, the dehydrogenation reaction was carried out in a three round neck flask. The hydrogenated solution was poured inside the flask, sealed and purged with a nitrogen gas. In these reactions, the
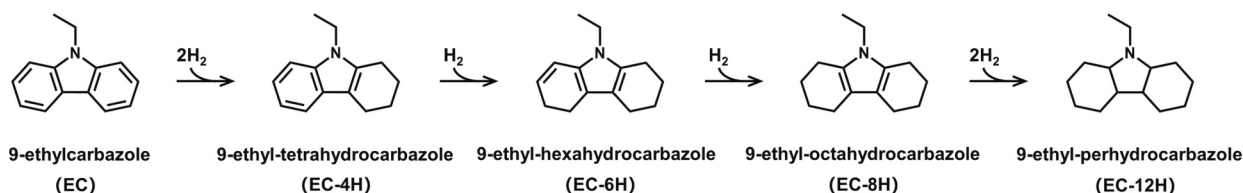
Scheme 1. Hydrogenation/dehydrogenation of EC.

products were analysed with a GC using Flame Ionization Detector (HP-5 column) and also with a GC–MS (Agilent QP 6890 N, Colum HP-5). After analysis of the hydrogenation mixture, dehydrogenation reactions were carried out with the product mixture resulting from hydrogenation, the same catalyst sample without being removed from the mixture and solvent (keeping constant 6 mL volume) in a two-neck round-bottom flask with a reflux condenser and an stripping N_2 flow $(0.1 \text{ mL/min}^{-1})$, at reflux temperature for 5 h. The course of the reaction was followed using the same GC and GC–MS as for the hydrogenation reaction.

3. Results and discussion

The samples under study were obtained starting from chitosan as precursor of N-doped graphitic carbon matrix embedding Ni NPs. They are denoted as Pt/Ni@(N)G-x in which (N)G refers to N-doped graphene and x indicates the Pt ppm content of the sample from 0 to 180,000 ppms (see Table 1). The preparation procedure is illustrated in Scheme 2. Chitosan is obtained from deacetylation of natural chitin that is the main waste of the fishery industry [28]. Upon protonation of glucosamine units chitosan becomes soluble in water [29]. Due to the formation of hydrogen bridges chitosan is able to adsorb significant amounts of metal salts in aqueous solution [30–33]. In addition, supercritical CO_2 drying favours high surface area and high porosity of the chitosan beads [34,35]. This porosity and particle morphology of chitosan is also inherited by the resulting graphitic carbon matrix derived therefrom [36]. It has been shown that upon pyrolysis under inert atmosphere chitosan, acting simultaneously as carbon and nitrogen source, becomes transformed into a N-doped graphitic carbon that can easily undergo almost complete exfoliation to single layer or few-layers N-doped defective graphene by sonication [37]. When chitosan contains adsorbed metal salts, spontaneous carbochemical reduction occurs during the pyrolysis, giving rise to metal NPs strongly grafted onto the graphene layers [38,39].

Following this procedure five different samples with similar Ni content from about 12 to 15 wt% and increasing Pt amounts from 0 to 0.18 wt% were prepared. Table 1 lists the samples under study, indicating their main analytical data including C and N contents. Note that, although all samples were intended to have the same Ni content, differing only on a minimum Pt amount, this is in practice undoable due to the differences in the exact amount of Ni^{2+} adsorbed onto chitosan and the unavoidable variations on the exact weight loss during chitosan pyrolysis. However, as seen in Table 1, the differences in the Ni, C and N composition of the series of samples are relatively minor.

The graphitic nature of the carbon matrix after pyrolysis was confirmed by Raman spectroscopy in which the expected 2D, G and D bands appearing, respectively, at 2800, 1590 and 1350 cm^{-1}

Table 1
Analytical composition, Ni average particle size and Pt content of the samples under study. CLs correspond to clusters.

Sample	Ni (wt %)[a]	Pt (wt %)[a]	C (wt %)[b]	N (wt %)[b]	Average Ni particle size (nm)[c]	Pt
Pt/Ni@(N)G-0	14.9	–	71.88	4.01	7.8 ± 1.4	–
Pt/Ni@(N)G-18	14.4	0.0018	73.75	3.49	7.7 ± 1.3	CL
Pt/Ni@(N)G-56	13.8	0.0056	70.17	3.48	7.8 ± 1.1	CLs
Pt/Ni@(N)G-450	12.6	0.0450	73.68	3.07	7.8 ± 1.6	CLs
Pt/Ni@(N)G-180000	12.3	0.18	73.90	3.10	–[d]	CLs

[a] Determined by ICP-AES analysis after dissolving the metals in aqua regia; [b] It is assumed that the difference to 100% is residual oxygen; [c] Determined from the DF-TEM images; [d] Fine Ni clusters dispersion with no measurable Ni NPs.

characteristic of defective graphitic carbon matrix were observed for all /the samples. Small differences were observed in the resolution of the 2D peaks at about 2700 cm^{-1} that were better resolved for samples Pt/Ni@(N)G-56, Pt/Ni@(N)G-450 and Pt/Ni@(N)G-180000, this being compatible with a lesser number of graphene layers stack in these samples. Fig. 1a presents the Raman spectra of the samples under study. Almost coincident Raman spectra have been reported earlier for the carbon residue derived from chitosan pyrolysis and attributed to the turbostratic defective graphitic carbon resulting from the thermal treatment [40]. The relative intensity of the G vs. the D band (I_G/I_D) that is a quantitative estimation of the density of defects on the graphene sheets. In the present case I_G/I_D is about 1.1 that is a common value previously measured for defective N-doped graphene from chitosan [40]. Interestingly, no peaks attributable to Ni—O appearing at about 540 cm^{-1} in the low frequency range in the Raman spectra could be recorded, indicating that the presence of Ni—O resulting from ambient oxidation of Ni metal should be negligible (see Fig. 1a) [41]. The absence of the characteristic vibrations of Ni—O bonds, meaning undetectable amounts of Ni oxides by Raman, will become relevant when assessing the relative contribution of Ni oxide/hydroxide observed by XPS analysis.

In fact, the crystal phase of Ni and the imperfect stacking of the graphitic layers was determined by XRD (Fig. 1b). As it can be seen in XRD, the peaks at 2Θ values of 44, 52, 76° corresponding to the 111, 200 and 220 facets of metallic fcc Ni phase were recorded for all the samples [42], together with a broad band at 24° corresponding to the loose stacking of disordered graphenic sheets in the graphitic residue [40]. The average particle size of Ni can be estimated from the broadness of the 111 peak by applying the Scherrer equation. These values have been collected in Table 1 and show that the Ni particle size is coincident within the error range for four samples and it is even smaller for Pt/Ni@(N)G-180000. No evidence for the presence of Pt could be obtained from XRD in good concordance with the trace amounts of this metal present in the samples.

The morphology of the samples was determined by field emission electron microscopy (FESEM). Fig. 2 shows selected FESEM images at two different magnifications to illustrate the morphology of one representative (Pt)Ni@(N)C catalyst, while Fig. S1 in supporting information contains a complete set of FESEM images. As it can be seen in these images, the Pt/Ni@(N)C samples are constituted by a coral-like, highly porous, spongy carbon matrix resulting from the transformation of linear polysaccharide fibrils into graphene sheets. No metal NPs could be visualized even at the highest magnification of the FESEM images, meaning that Ni particles should be smaller than the resolution of this microscopy technique, about 50 nm.

The presence of Ni NPs could be however clearly observed in dark-field transmission electron microscopy (DF-TEM) that also reveals the interaction of these Ni NPs with the graphene layers and the distribution of Pt (Figs. 3 and 4 and Fig. S2). As it.

can be seen by DF-TEM, metal NPs appear as bright spots in the carbon matrix background. DF-TEM images also show a bright background without clear observable particles, meaning that besides the larger NPs, the Ni metal is also highly dispersed throughout the N-doped graphitic matrix as small clusters with dimensions smaller than 2 nm, below the resolution of our DF-TEM technique, leading to a bright background. Some preferential location of these small Ni clusters at the rims and wrinkles of the graphene support was observed. The average particle size of the Ni NPs without considering these small clusters was determined by measuring the diameter of a statistically relevant number of these Ni NPs with measurable dimensions. Table 1 collects the mean diameters of these metal NPs. Note that these mean diameters are over estimated, since they do not consider the Ni clusters that are observed as bright contrast in the DF-TEM images, but whose number and size cannot be measured. As an example, sample Pt/Ni@(N)G-180000 did not present many Ni NPs and DF-TEM images show that in sample Pt/Ni@(N)G-180000 Ni is very well dispersed as ultrafine Ni NPs
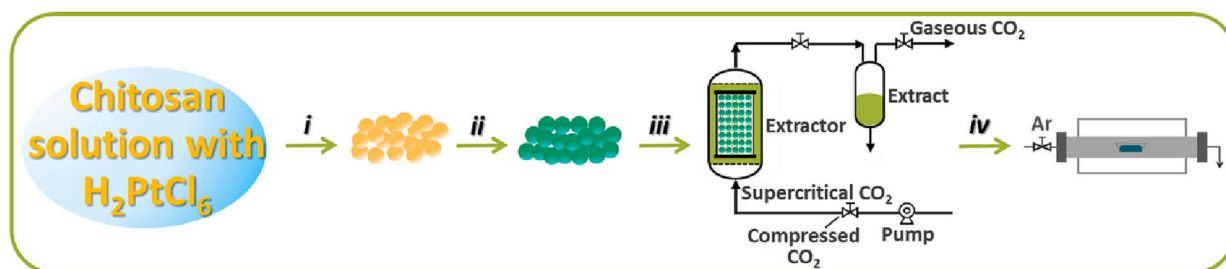
Scheme 2. Procedure used to prepare the Pt/Ni@(N)C samples under study. i) precipitation in KOH solution; ii) water/ethanol exchange and Ni(OAc)$_2$ impregnation; iii) supercritical CO$_2$ drying; iv) pyrolysis in Ar atmosphere.
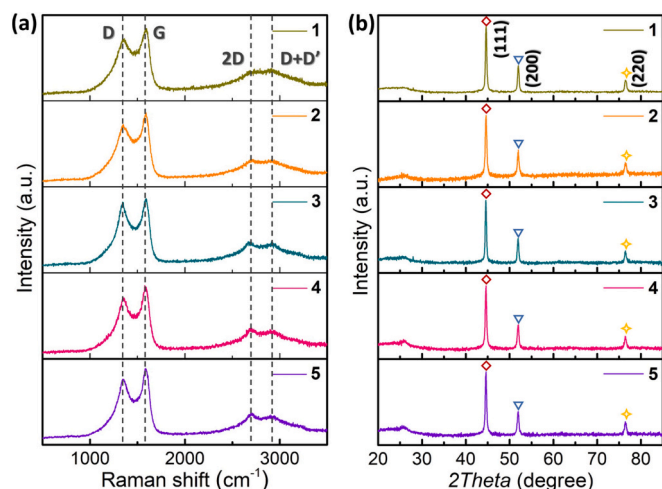
Fig. 1. Raman spectra recorded upon laser excitation at 414 nm (a) and powder XRD patterns of samples Pt/Ni@(N)G-x (b). 1: Pt/Ni@(N)G-0, 2: Pt/Ni@(N)G-18, 3: Pt/Ni@(N)G-56, 4: Pt/Ni@(N)G-450, 5: Pt/Ni@(N)G-180000. The labels D, G, 2D and G + G' in part (a) correspond to the *defect, graphitic* and *overtones* of the defect bands. Part (b) indicates the plane diffraction of the main peaks.
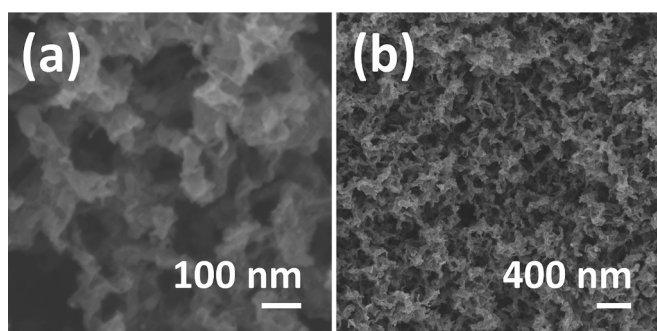
Fig. 2. FESEM images of sample Pt/Ni@(N)G-18 at two different magnifications as indicated in the scale bars showing the large porosity and spongy morphology of (N)G support and the absence of large Ni nanoparticles (NPs).

throughout the carbon matrix with very few countable metal NPs. For this sample Pt/Ni@(N)G-180000, it was not possible to determine the Ni particle size and, therefore, this sample is denoted in footnote "d" of Table 1 as constituted by Ni clusters. In those cases in which Ni NPs were observed, as it happens in sample Pt/Ni@(N)G-18, high-resolution transmission electron microscopy (HRTEM) images (Fig. 4) allow to measure the interplanar distance of the Ni NPs as 0.203 nm that agrees with the 111 plane diffraction peak in XRD.

Importantly, these HRTEM images show that the periphery of several of these Ni NPs are incompletely surrounded by three/four graphene

layers (see Fig. 4 a that has highlighted the graphene layers, but they can also be seen in Fig. 4 b), suggesting an intimate Ni-graphene contact as it has been observed in related (metal NP)/graphene support samples prepared analogously [26]. Although similar details cannot be obtained for small Ni NPs due to resolution limitations, it is assumed that an intimate contact should occur also for them. This assumption is also supported by the lattice matching between the 111 facet of Ni film [43] and graphene that is the base of the chemical vapour deposition graphene film growth and also in the facet orientation of nascent Au and Cu NPs developed on preformed graphene sheets [39]. It is proposed that this Ni/(N)G interaction is important in the control of the electronic density of the Ni NPs and also to provide stabilization against particle growth under catalytic reactions. Precedents in the literature (both experimentally [44–46] and theoretically [47–49]) have shown that pyridinic and graphenic N atoms establish a strong interaction with transition metal atoms supported on graphene and it is likely that a similar effect happens here.

From energy-dispersive X-ray spectroscopy (EDS) analysis, the presence of the metal elements, Ni and Pt, could be determined for the samples with the highest Pt percentage by electron microscopy. Of note is that although the Pt content is very low in every sample, the high atomic weight of this heavy transition metal makes easier its detection and quantification, even as ultrafine (sub)nanometric particles, for samples with the highest Pt content. For these samples with the highest Pt content, even in minute amounts, particle size was just at the detection limit of our instrument, meaning that they should be below a few nm. A good dispersion of Pt throughout the graphitic carbon matrix was observed by EDS analyses. Interestingly, although EDS elemental mapping shows that Pt and Ni are not associated, in a few high-resolution images it was possible to detect Pt NPs in contact Ni NPs (see Fig. 4 b). Figs. S3 and S4 show representative TEM images and EDS analysis of the samples under study in which the location of Pt and the larger Ni particles have been highlighted. EDS analyses around Ni NPs also show that C proportion increases at their periphery in agreement with the partial wrapping of Ni by the graphenic matrix. Furthermore, analysis of the electron diffraction indicates that the particles are constituted by Ni metal, with some accumulation of NiO at the periphery of the NP.

To further address Pt distribution on (N)G support five additional samples, denoted as Pt@(N)G-x, lacking Ni but containing Pt at similar percentages as those in samples Pt/Ni@(N)G-x, were also prepared. The analytical data of these Pt@(N)G-x samples are collected in Table S2 of the supporting information and, although not exactly with the same Pt values as Pt/Ni@(N)G-x, they are almost coincident percentages. DF-TEM images of the Pt@(N)G-14 are presented in Fig. S5 of the supporting information and they show the absence of Pt NPs. This suggests that also for the Pt/Ni@(N)G-18 sample, Pt should be distributed as small clusters.

The elements present on the surface of the Pt/Ni@(N)G catalysts, their oxidation states and the distribution among different coordination spheres were analysed by XPS. Fig. 5 presents the results for the most active sample. As expected, the presence of C, N, O, Ni and Pt was detected. For sample Pt/Ni@(N)G-18, deconvolution of the high
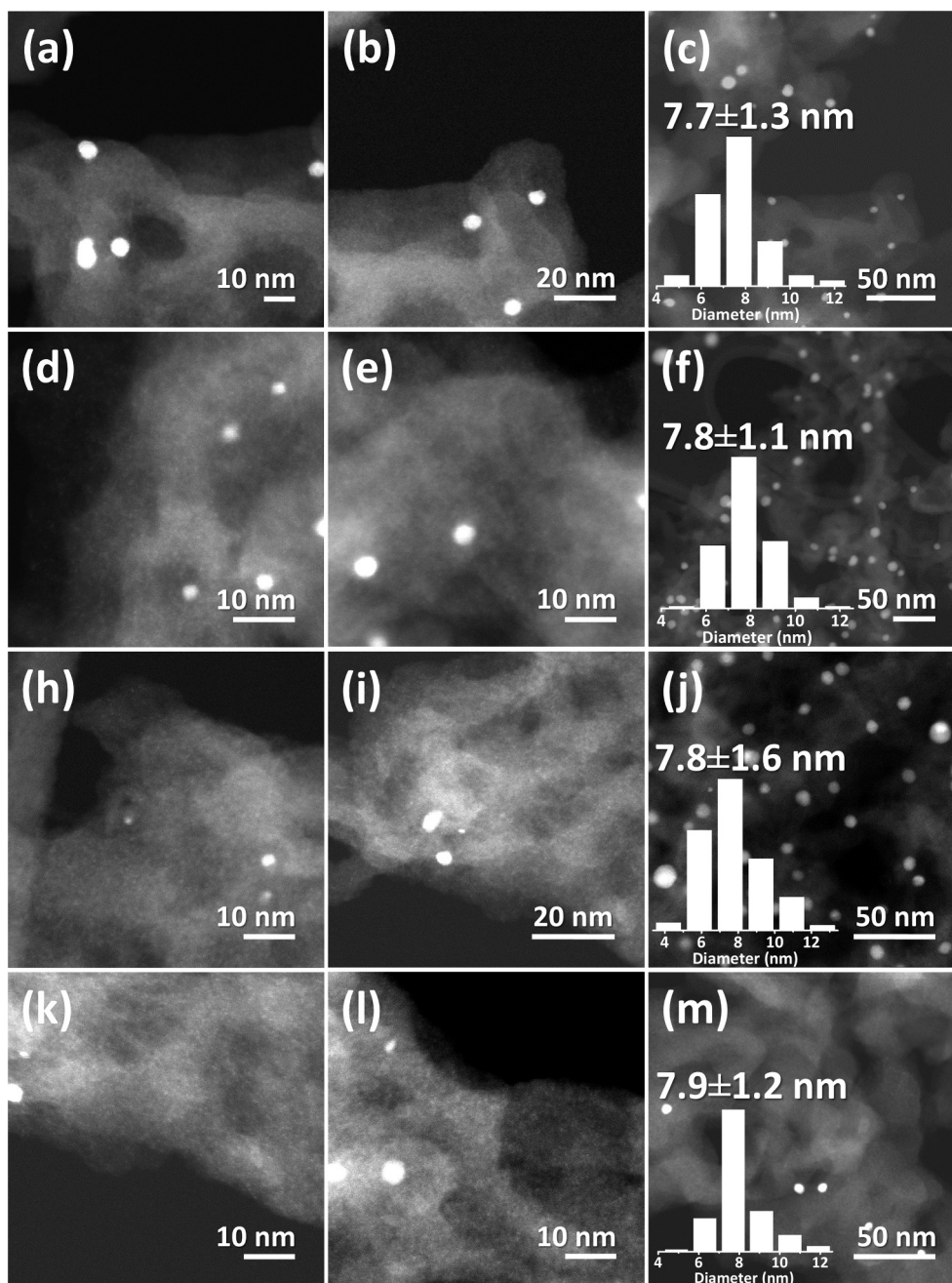
Fig. 3. DF-TEM images of samples Pt/Ni@(N)G-18 (a,b,c), Pt/Ni@(N)G-56 (d,e,f), Pt/Ni@(N)G-450 (h,i,j) and Pt/Ni@(N)G-180000 (k,l,m). The insets of frames c,f,j and m correspond to the histograms of Ni particle size distribution with indication of the average particle size and the standard deviation.

resolution XPS C 1 s peak shows a major contribution corresponding to graphitic carbon at 285.4 eV accompanied with two minor components attributable to C bonded to O or N with single or double bonds and C atoms of carboxylate groups appearing at 285.8, 286.5 and 289.3 eV, respectively. XPS N 1 s peak presents three components at 399.1, 401.1 and 403.5 eV that can be assigned, respectively, to N atoms in a pyridinic, graphitic and pyridinic N-oxide coordination. The presence in N-doped graphene of residual O from the chitosan precursor in a percentage about 8 wt% as detected in XPS by the O 1 s peaks at 531.2, 532.2, 533.2 and 534.1 eV corresponding to metal oxide, C═O, O bonded to C or N and carboxylate groups, respectively, was also observed. These C, N and O atom distributions agree well with the expected components and binding energies reported for C, N and O in N-doped graphitic materials. [40]

The oxidation state and coordination distribution of Ni element is always difficult to interpret in XPS, due to the complexity of the peaks corresponding to its 2p core orbitals. In the present case, the experimental XPS Ni 2p peak could be satisfactorily deconvoluted in two families at 854.6 and 861.8 eV that can be ascribed to metallic Ni and Ni oxide/hydroxide, respectively. Comparison with literature data shows that these binding energies are notably upshifted respect to the common values for metallic Ni 2p (852.6 eV) or NiO (853.7 eV) [50,51], implying that N-doped graphene support is removing charge density to the metal. In the case of Ni/Al$_2$O$_3$ the Ni 2p binding energy values were reported as 852.8 and 856.3 eV for the Ni metal and oxide/hydroxide, respectively, thus confirming the notable influence of the N-doped graphene support on the electron density of the Ni species [52]. Also noteworthy is the fact that while XRD patterns only indicates the presence of metallic Ni NPs and Raman spectroscopy does not detect the presence of Ni—O bonds, XPS analysis is able to detect NiO on the surface of the metal NPs, in
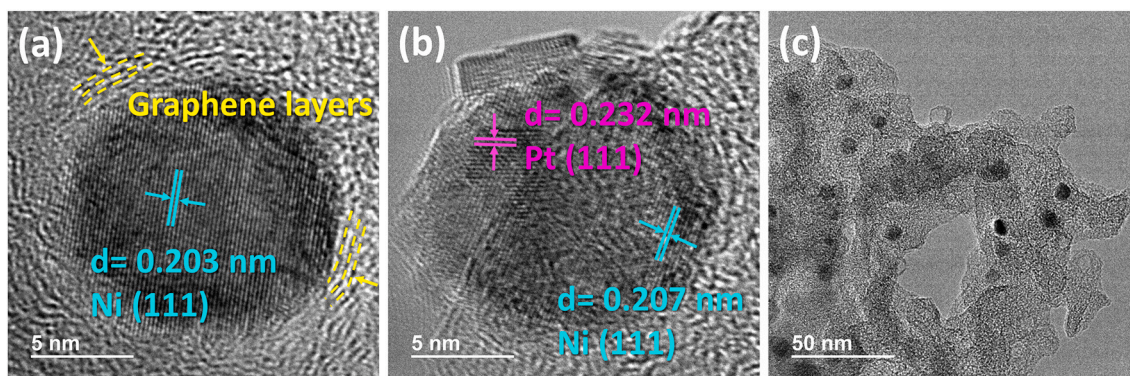
Fig. 4. HRTEM images of sample Pt/Ni@(N)G-18 at two different magnifications (see scale). The presence of graphene layers wrapping the Ni NP has been indicated (a) as well as the interplanar distances corresponding to the Ni (111) planes (a and b) and Pt (111) (b).
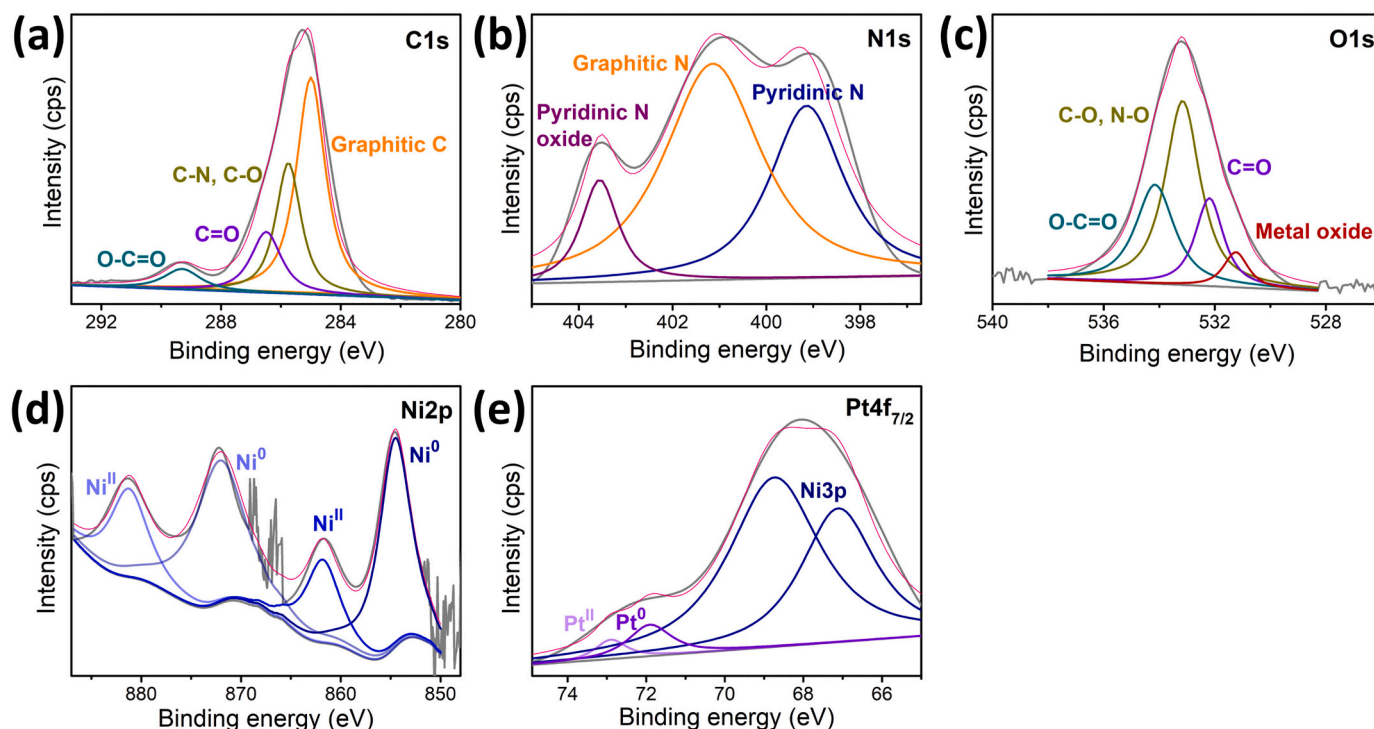

Fig. 5. XPS analysis and corresponding best deconvolution of the core levels (element as indicated in the plot) for sample Pt/Ni@(N)G-18.

agreement with the electron diffraction information for the Ni NPs obtained in high resolution TEM. To reconcile all the information from spectroscopy and microscopy, it has to be admitted that the presence of Ni oxides/hydroxides has to be limited to a thin outer layer of the Ni particles. Partial oxidation of the external surface of metal NPs is a fact commonly encountered in supported metal NPs and indicates a certain degree of spontaneous surface passivation due to sample oxidation by exposure to the ambient [39].

Importantly, the presence in XPS of the Pt 4f peak was also observed. The experimental peak in the Pt 4f region could be fitted to four components appearing at 67.1, 68.7, 71.9 and 72.9 eV, in which peaks 67.1, 68.7 eV belong to the emission lines of Ni 3p peak. The binding energy values of Pt 4f can be assigned to Pt^0 and $Pt(OH)_2$ that are typically reported at 70.9 and 72.9 eV, respectively, for Pt NPs [53]. The notable upshift experienced by Pt^0 is understandable considering its high dispersion on the sample, with very different coordination than the metallic or oxide state. In addition, as in the case of Ni atoms, the upshift Pt binding energy values means a charge density transfer from the Pt to

(N)C support, as it was reported in the case Pt single atoms supported on N-doped carbon black [54]. Importantly, for Ni alloys of diluted Pt, a shift of 0.5 eV in opposite directions downshifting the Ni 2p binding energy and upshifting the Pt 4f peak has been reported [55]. The fact that in the present samples both XPS peaks of Ni and Pt are largely upshift is compatible with our proposal that interaction with the (N)C support in larger weight percentage is the dominant factor prevailing over other possible effects. In addition, the large shift indicates a strong grafting of the Pt/Ni NPs on the (N)C as it has been observed in the case of Au [56].

As commented in the introduction the purpose of the present study is to determine the increase in the efficiency of a Ni-based catalyst by minimal amounts of Pt as promoter. It is expected that the high Pt dispersion according to TEM images should largely influence the catalytic activity of Ni@(N)C.

Aimed at evaluating the leading concept of this study, the series of Pt/Ni catalysts were initially tested for the hydrogenation of EC. The reactions were carried out at 200 °C under a H_2 pressure of 40 bar using

30 mg catalyst and 50 mg EC dissolved with 6 mL cyclohexane. Starting from EC, disappearance of EC over the time was accompanied with the concomitant formation of a mixture of hydrogenation products (Scheme 1). According to mass spectrometry, the major products correspond to the addition of 4 (EC-4H), 8 (EC-8H) and 12 (EC-12H) hydrogen atoms. Similar products were reported in the literature employing of supported Ru catalysts [8]. The results are summarized in Table 2 and presented graphically in Fig. 6. It was observed that sample Pt/Ni@(N)G-0 containing only Ni exhibited the lowest catalytic activity, although higher than other reported Ni catalysts. In the case of Ni/SiO$_2$ it has been reported high Ni/EC ratios above 10% to achieve high EC conversions [57]. It seems that (N)C as support and the strong grafting of the Ni NPs on it would be a crucial factor increasing the catalytic activity of the Ni metal. In this regard, the clear change in the XPS binding energy values for Ni and Pt towards higher values is in line with an influence of the catalytic activity towards hydrogenation/dehydrogenation by electron density transfer from Ni to the (N)C support.

The presence of Pt in the composition of the Ni@(N)C catalyst increased EC conversion, although the catalytic activity does not grow linearly with the Pt content.

As it can be seen in Fig. 6a, the catalytic activity in terms of EC conversion and H$_2$ storage capacity does not correlate with the amount of Pt in the sample, the most active catalyst being sample Pt/Ni@(N)G-18 that contains the lesser Pt amount. Essentially a complete H$_2$ storage capacity (5.8 wt%) was achieved for Pt/Ni@(N)G-18, with the minimal Pt content under the reaction conditions. As controls to determine the intrinsic Pt activity, five analogous Pt@(N)C-x samples, lacking Ni, were also tested. The results are presented in Fig. S6 in the supporting information. For the Pt@(N)C-140000 sample with 0.14% Pt a hydrogen storage activity in EC under the reaction conditions of 0.5% was reached, while for the Pt@(N)C-18 corresponding to the optimal Pt loading the hydrogen storage activity in EC was essentially 0%.

The reaction rate for Pt/Ni@(N)G-18 appears to be 4.05 times faster than that for sample Pt/Ni@(N)G-0 containing Ni exclusively. Apart from Pt/Ni@(N)G-18, there seems to be a linear correlation between the Pt content and the H$_2$ storage capacity reached for the other samples from Pt/Ni@(N)G-56 to Pt/Ni@(N)G-180000 (Fig. 6a) Although, for a different reaction and Pd atoms in a 3D *S*-methyl cysteine-derived metal-organic framework, an analogous uncommon trend in the promotion of the catalytic activity has been reported in the literature for the case of Pd and it was interpreted considering that the sample with the lowest Pd concentration corresponds to the case of single Pd atoms, while the decrease in the catalytic activity at higher Pd loadings was due to formation of Pd clusters [58]. In the present case, our TEM resolution does not allow observing single atoms and Pt NPs were not formed in the range of loadings under study. Therefore, based on the catalytic results it is proposed that Pt/Ni@(N)G-18 could have a higher-than-expected

activity due to the prevalence of a different Pt distribution regime in small clusters, while in the samples from Pt/Ni@(N)G-56 to Pt/Ni@(N)G-180000, the activity could arise from Pt NPs. An analogous claim was also made for the influence of single Rh atoms to justify the high catalytic activity of Rh (0.1 wt%) on Ni/γ-Al$_2$O$_3$. [13] To provide some support to our proposal and visualize better the Pt distribution on (N)G, the analogous Pt@(N)G-18 sample lacking Ni NPs previously used for the catalytic controls was analysed by high-resolution dark-field TEM. As it can be seen in Fig. S5 of the supporting information, the images for this Pt@(N)G-18 control sample show the absence of Pt NPs on a bright background, thus, supporting the presence of small Pt nanocluster in these Pt/Ni@(N)G-18 sample containing minute Pt loading.
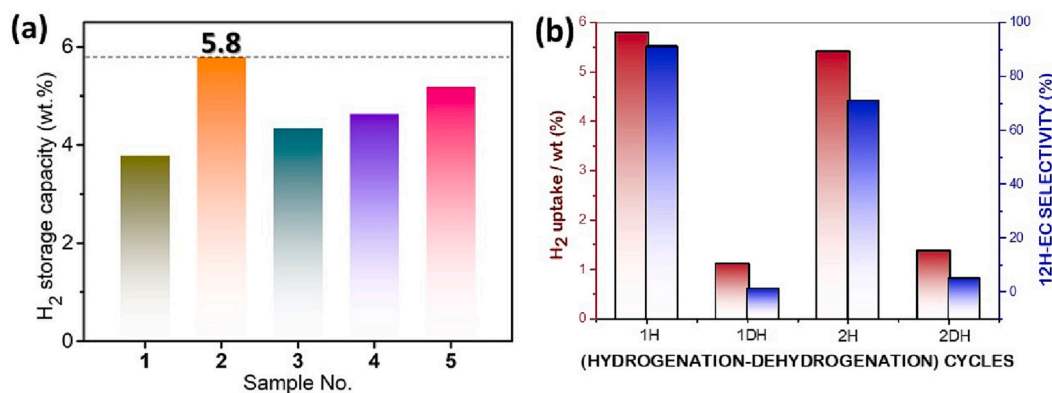
Regarding the Ni particle size, a particular comment deserves sample Pt/Ni@(N)G-180000 that contains the highest Pt loading and in which the Ni metal is very well dispersed as clusters. It seems that this high Ni dispersion does not play a significant role in its catalytic activity that follows the expected trend as the other Pt/Ni@(N)C samples. Incidentally, the influence of Rh at 10000 ppm decreasing the particle size of Ni NPs has been previously reported [13] and a similar effect could take place here for the Pt/Ni@(N)G-180000 sample with the highest Pt loading.

Table 2 also shows the product distribution for each of the catalysts. Worth noting is that although eight pair of stereoisomers could be possible for EC-12H, GC analyses indicates the preferential formation of 4 major products in accordance with the literature. [14].

To put the catalytic activity of Pt/Ni@(N)G-18 into a broader context, its performance was compared with data reported in the literature for EC hydrogenation for other catalysts. This survey is presented in Table S3 of supporting information. While several catalysts are based on Ru or noble metals, comparison with Ni NPs supported on alumina deserves a special comment. Although comparison of catalytic performance under different reaction conditions should be taken cautiously, in the case of Ni/Al$_2$O$_3$, EC conversion at 160 °C and 70 bar H$_2$ was 70% with only 55% selectivity towards EC-12H [13]. Addition of 10,000 ppms Rh (0.1%, Rh as single atoms) increases EC conversion and selectivity to EC-12H, reaching the maximum hydrogen storage capacity for EC, similar to the 5.8 wt% measured here for three orders of magnitude lower noble metal loading. This comparison illustrates the remarkable performance of Pt/Ni@(N)G-18.

To understand the role of Pt on the Ni, providing evidence on the better H$_2$ activation by Pt in minute amounts, H$_2$ adsorption measurements were performed for samples Pt/Ni@(N)G-0 (lacking Pt) and Pt/Ni@(N)G-18 the best performing catalyst. As it can be seen in Fig. 7, contrasting H$_2$ physi- and chemisorption profiles were measured for both samples. Compared to sample Pt/Ni@(N)G-0, H$_2$ chemisorption was observed for sample Pt/Ni@(N)G-18 at low pressures, even though the measurements determine that the final Ni dispersion (1.85%) and Ni surface area (1.78 m$^2 \times$ g^{-1}) are very similar for the two samples. This is in agreement with the known activity of Pt to activate H$_2$ [59].

According to Scheme 1, the use of EC as LHOC would require H$_2$ release in the automobile through a less-studied dehydrogenation process of the mixture resulting from EC hydrogenation. To see the activity of sample Pt/Ni@(N)G-18 as H$_2$ release catalyst, the mixture resulting from EC hydrogenation at 5.8 wt.% H$_2$ storage capacity was submitted without any purification to dehydrogenation at 200 °C under a N$_2$ stripping. The results are presented in Fig. 6b showing a considerable decrease in EC-12H and the prevalence of EC in 60% yield accompanied by a 30% of EC-8H and some minor EC-4H. Up to 4.5 wt% H$_2$ release was achieved. Another consecutive hydrogenation/dehydrogenation cycle was performed by the same catalyst Pt/Ni@(N)G-18 with the mixture derived from the first hydrogenation-dehydrogenation cycle. Some decay in the H$_2$ storage capacity up to 5.3 wt% was observed and the subsequent dehydrogenation cycle released 4.0 wt% H$_2$. This diminution in the H$_2$ storage capacity was accompanied by a gradual variation in the product distribution, decreasing the final proportion of EC-12H (hydrogenation step) and EC (dehydrogenation cycle), while

Table 2

Hydrogen storage capacity in EC hydrogenation and different product distributions achieved for the series of Pt/Ni@G(N)-x catalysts. The maximum hydrogen storage capacity of EC corresponding to an increase of 5.8% in weight. Reaction conditions: catalyst 30 mg, temperature 200 °C, pressure 40 bar, 50 mg EC, cyclohexane as solvent (6 mL), time 5 h. EC, EC-4H, EC-8H and EC-12H refer to N-ethylcarbazole (EC) hydrogenation products in which 4, 8 or 12H atoms, respectively, have been incorporated.

Sample No.	H$_2$ storage capacity (wt%)	EC (%)	EC-4H (%)	EC-8H (%)	EC-12H (%)
Pt/Ni@(N)G-0	3.79	25.4	27.3	8.7	19.6
Pt/Ni@(N)G-18	5.80	0	0.3	8.5	91.2
Pt/Ni@(N)G-56	4.35	22.0	33.2	7.8	20.6
Pt/Ni@(N)G-450	4.64	20.0	49.1	7.4	23.6
Pt/Ni@(N)G-180000	5.20	10.2	54.0	8.0	27.8

Fig. 6. H$_2$ storage capacity in EC hydrogenation achieved for catalysts Pt/Ni@(N)G-x catalysts (a, samples 1, 2, 3, 4 and 5 refer to Pt/Ni@(N)G-0, Pt/Ni@(N)G-18, Pt/Ni@(N)G-56, Pt/Ni@(N)G-450 and Pt/Ni@(N)G-180000, respectively) and H$_2$ uptake in EC (in wt%, red bars, left axis) and EC-12H selectivity (in product %, blue bars, right axis) in two consecutive EC hydrogenation 1H and 2H)-dehydrogenation (1DH and 2DH) cycles using the same Pt/Ni@(N)G-18 sample (b). Reaction conditions: a) Hydrogenation: catalyst 30 mg, temperature 200 °C, pressure 40 bar, cyclohexane as solvent, time 5 h; b) Dehydrogenation: the product mixture resulting from hydrogenation, the same Pt/Ni@(N)G-18 without treatment, cyclohexane (6 mL), reflux temperature, stripping N$_2$ flow, 5 h. (For interpretation of the references to colour in this figure legend, the reader is referred to the web version of this article.)
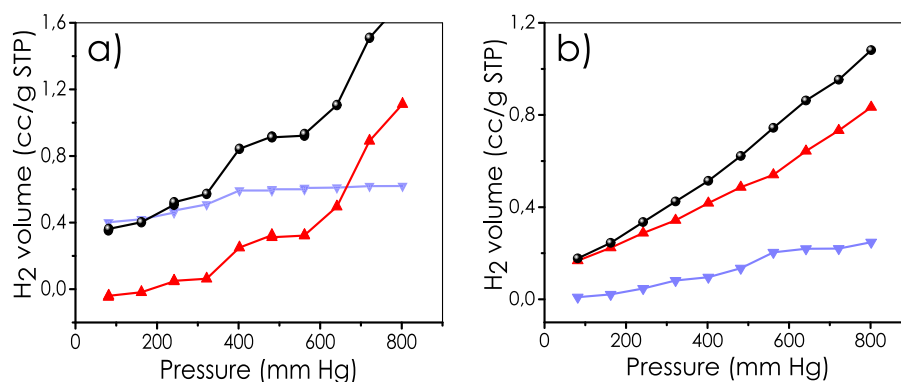
Fig. 7. Hydrogen adsorption measurements showing the contrasting profiles, particularly for chemisorption curve at low pressure, of Pt/Ni@(N)G-18 (a) and Pt/Ni@(N)G-0 lacking Pt (b). The plots indicates the amount of hydrogen physisorbed (▲, red line), chemisorbed (▼, blue line) and total adsorption (●, black line) for these two samples. (For interpretation of the references to colour in this figure legend, the reader is referred to the web version of this article.)

increasing the proportions of other products with intermediate H$_2$ content, particularly EC-8H. This fatigue is due to the contribution of two different factors, namely, the formation of EC derivative products that undergo more difficult hydrogenation/dehydrogenation cycling and catalyst deactivation. Starting from pure EC, hydrogenation renders a product distribution with four major EC-12H but constituted by a mixture of detectable products, although some of them in very minute proportion. The four hydrogenation/dehydrogenation cycles increase the complexity of the mixture, and it is reasonable to expect that some of these minor compounds will increase their proportion over cycling and they could be less prone to react than the major products of the process.

Catalyst deactivation was assessed by reusing the Pt/Ni@(N)C sample after four hydrogenation/dehydrogenation cycles with the same EC batch with a new pure EC feedstock and observing an almost coincident H$_2$ storage capacity of 5.8 wt% and product distribution with pure EC as the fresh catalyst. In addition, this sample after exhaustive use was analysed by XRD, TEM and XPS analysis (see Fig. S7 in supporting information), observing no changes in the XRD pattern, Ni average particle size distribution and Ni 2p peak. In addition, chemical analyses of the reused solid reveal a similar Pt content in the sample.

4. Conclusions

Pyrolysis of Ni(OAc)$_2$ embedded within chitosan renders graphitic carbon residues containing Ni NPs of narrow particle size distribution about 8 nm and with loadings about 15 wt%. The resulting Ni@(N)C appears to be an effective catalyst for EC hydrogenation, compared to the reports of Ni NPs supported on metal oxides. Addition of minute Pt amounts on Ni@(N)C increases significantly their activity as hydrogenation/dehydrogenation catalysts for H$_2$ storage and release on EC. Importantly, in the range of minimal Pt amounts studied, there is not a linear relationship between the Pt loading and the increase in catalytic activity. Following a previous report in the case of Pd, it is proposed that at the lowest Pt concentration, Pt distribution in small clusters increases the efficiency as catalysts, while somewhat higher Pt amounts correspond to a different regime with small Pt NPs and somewhat lower catalytic activity. A gradual decrease in the H$_2$ storage/release activity for reused EC mixtures was observed. However, this activity decay is not attributable exclusively to the performance of the Pt/Ni@(N)C catalyst, since using pure EC feedstock restores most of the H$_2$ storage capacity for the five-times reused Pt/Ni@(N)C sample, indicating that the fatigue in the system is also due to the formation upon hydrogenation/dehydrogenation cycling of intermediate products with lesser reactivity.

Declaration of Competing Interest

None.

Data availability

Data will be made available on request.

Acknowledgements

Appendix A. Supplementary data

Supplementary data to this article can be found online at https://doi.org/10.1016/j.catcom.2023.106641.

References

[1] W. McDowall, M. Eames, Forecasts, scenarios, visions, backcasts and roadmaps to the hydrogen economy: a review of the hydrogen futures literature, Energy Policy 34 (2006) 1236–1250.

[2] J.O. Abe, A. Popoola, E. Ajenifuja, O. Popoola, Hydrogen energy, economy and storage: review and recommendation, Int. J. Hydrog. Energy 44 (2019) 15072–15086.

[3] H. Kasai, A.A.B. Padama, B. Chantaramolee, R.L. Arevalo, Review of the current status of the hydrogen economy, in: Hydrogen and Hydrogen-Containing Molecules on Metal Surfaces, Springer, 2020, pp. 119–147.

[4] P.T. Aakko-Saksa, C. Cook, J. Kiviaho, T. Repo, Liquid organic hydrogen carriers for transportation and storing of renewable energy–review and discussion, J. Power Sources 396 (2018) 803–823.

[5] T. He, Q. Pei, P. Chen, Liquid organic hydrogen carriers, J. Energy Chem. 24 (2015) 587–594.

[6] P.M. Modisha, C.N. Ouma, R. Garidzirai, P. Wasserscheid, D. Bessarabov, The prospect of hydrogen storage using liquid organic hydrogen carriers, Energy Fuel 33 (2019) 2778–2796.

[7] P. Modisha, P. Gqogqa, R. Garidzirai, C.N. Ouma, D. Bessarabov, Evaluation of catalyst activity for release of hydrogen from liquid organic hydrogen carriers, Int. J. Hydrog. Energy 44 (2019) 21926–21935.

[8] K.M. Eblagon, D. Rentsch, O. Friedrichs, A. Remhof, A. Zuettel, A. Ramirez-Cuesta, S.C. Tsang, Hydrogenation of 9-ethylcarbazole as a prototype of a liquid hydrogen carrier, Int. J. Hydrog. Energy 35 (2010) 11609–11621.

[9] L. Zhou, L. Sun, L. Xu, C. Wan, Y. An, M. Ye, Recent developments of effective catalysts for hydrogen storage technology using N-Ethylcarbazole, Catalysts 10 (2020) 648.

[10] P.C. Rao, M. Yoon, Potential liquid-organic hydrogen carrier (LOHC) systems: a review on recent progress, Energies 13 (2020) 6040.

[11] Y. Sekine, T. Higo, Recent trends on the dehydrogenation catalysis of liquid organic hydrogen carrier (LOHC): a review, Top. Catal. (2021) 1–11.

[12] K. Morawa Eblagon, K. Tam, K.K. Yu, S.-L. Zhao, X.-Q. Gong, H. He, L. Ye, L.-C. Wang, A.J. Ramirez-Cuesta, S.C. Tsang, Study of catalytic sites on ruthenium for hydrogenation of N-ethylcarbazole: implications of hydrogen storage via reversible catalytic hydrogenation, J. Phys. Chem. C 114 (2010) 9720–9730.

[13] H. Liu, C. Zhou, W. Li, W. Li, M. Qiu, X. Chen, H. Wang, Y. Sun, Ultralow Rh bimetallic catalysts with high catalytic activity for the hydrogenation of N-ethylcarbazole, ACS Sustain. Chem. Eng. 9 (2021) 5260–5267.

[14] K.M. Eblagon, K. Tam, S.C.E. Tsang, Comparison of catalytic performance of supported ruthenium and rhodium for hydrogenation of 9-ethylcarbazole for hydrogen storage applications, Energy Environ. Sci. 5 (2012) 8621–8630.

[15] M. Yang, Y. Dong, S. Fei, H. Ke, H. Cheng, A comparative study of catalytic dehydrogenation of perhydro-N-ethylcarbazole over noble metal catalysts, Int. J. Hydrog. Energy 39 (2014) 18976–18983.

[16] S. Fei, B. Han, L. Li, P. Mei, T. Zhu, M. Yang, H. Cheng, A study on the catalytic hydrogenation of N-ethylcarbazole on the mesoporous Pd/MoO3 catalyst, Int. J. Hydrog. Energy 42 (2017) 25942–25950.

[17] F. Sotoodeh, L. Zhao, K.J. Smith, Kinetics of H2 recovery from dodecahydro-N-ethylcarbazole over a supported Pd catalyst, Appl. Catal. A Gen. 362 (2009) 155–162.

[18] C. Wan, Y. An, F. Chen, D. Cheng, F. Wu, G. Xu, Kinetics of N-ethylcarbazole hydrogenation over a supported Ru catalyst for hydrogen storage, Int. J. Hydrog. Energy 38 (2013) 7065–7069.

[19] Y. Wu, H. Yu, Y. Guo, Y. Zhang, X. Jiang, B. Sun, K. Fu, J. Chen, Y. Qi, J. Zheng, Promoting hydrogen absorption of liquid organic hydrogen carriers by solid metal hydrides, J. Mater. Chem. A 7 (2019) 16677–16684.

[20] H. Yu, X. Yang, Y. Wu, Y. Guo, S. Li, W. Lin, X. Li, J. Zheng, Bimetallic Ru-Ni/TiO2 catalysts for hydrogenation of N-ethylcarbazole: role of TiO2 crystal structure, journal of energy, Chemistry 40 (2020) 188–195.

[21] A. Ali, U. Kumar, H.J. Lee, Catalytic hydrogenation and dehydrogenation performance of 9-ethylcarbazole as a liquid organic hydrogen carrier, J. Mech. Sci. Technol. 33 (2019) 5561–5569.

[22] P. Serna, P. Concepción, A. Corma, Design of highly active and chemoselective bimetallic gold–platinum hydrogenation catalysts through kinetic and isotopic studies, J. Catal. 265 (2009) 19–25.

[23] P. Serna, A. Corma, Transforming nano metal nonselective particulates into chemoselective catalysts for hydrogenation of substituted nitrobenzenes, ACS Catal. 5 (2015) 7114–7121.

[24] P. Serna, M. Boronat, A. Corma, Tuning the behavior of au and Pt catalysts for the chemoselective hydrogenation of nitroaromatic compounds, Top. Catal. 54 (2011) 439–446.

[25] L. Peng, B. Jurca, A. Primo, A. Gordillo, V.I. Parvulescu, H. García, Co–Fe clusters supported on N-doped graphitic carbon as highly selective catalysts for reverse water gas shift reaction, ACS Sustain. Chem. Eng. 9 (2021) 9264–9272.

[26] B. Jurca, L. Peng, A. Primo, A. Gordillo, V.I. Parvulescu, H. García, Co–Fe nanoparticles wrapped on N-doped graphitic carbons as highly selective CO2 Methanation catalysts, ACS Appl. Mater. Interfaces 13 (2021) 36976–36981.

[27] D. Mateo, J. Albero, H. Garcia, Graphene supported NiO/Ni nanoparticles as efficient photocatalyst for gas phase CO2 reduction with hydrogen, Appl. Catal. B Environ. 224 (2018) 563–571.

[28] M.N.R. Kumar, A review of chitin and chitosan applications, React. Funct. Polym. 46 (2000) 1–27.

[29] S.K. Shukla, A.K. Mishra, O.A. Arotiba, B.B. Mamba, Chitosan-based nanomaterials: a state-of-the-art review, Int. J. Biol. Macromol. 59 (2013) 46–58.

[30] M. Vakili, S. Deng, G. Cagnetta, W. Wang, P. Meng, D. Liu, G. Yu, Regeneration of chitosan-based adsorbents used in heavy metal adsorption: a review, Sep. Purif. Technol. 224 (2019) 373–387.

[31] M.B. Kasiri, Application of chitosan derivatives as promising adsorbents for treatment of textile wastewater, in: The Impact and Prospects of Green Chemistry for Textile Technology, 2019, pp. 417–469.

[32] A.J. Al-Manhel, A.R.S. Al-Hilphy, A.K. Niamah, Extraction of chitosan, characterisation and its use for water purification, J. Saudi Soc. Agric. Sci. 17 (2018) 186–190.

[33] R. Yang, H.L. Li, M. Huang, H. Yang, A. Li, A review on chitosan-based flocculants and their applications in water treatment, Water Res. 95 (2016) 59–89.

[34] A. El Kadib, M. Bousmina, Chitosan bio-based organic–inorganic hybrid aerogel microspheres, Chem Eur J 18 (2012) 8264–8277.

[35] A. El Kadib, Green and functional aerogels by macromolecular and textural engineering of chitosan microspheres, Chem. Rec. 20 (2020) 753–772.

[36] S. Frindy, A. Primo, H. Ennajih, R. Bouhfid, M. Lahcini, E.M. Essassi, H. Garcia, A. El Kadib, Chitosan–graphene oxide films and CO2-dried porous aerogel microspheres: interfacial interplay and stability, Carbohydr. Polym. 167 (2017) 297–305.

[37] H. Kaczmarek, J. Zawadzki, Chitosan pyrolysis and adsorption properties of chitosan and its carbonizate, Carbohydr. Res. 345 (2010) 941–947.

[38] G. Abellan, M. Latorre-Sanchez, V. Fornes, A. Ribera, H. García, Graphene as a carbon source effects the nanometallurgy of nickel in Ni, Mn layered double hydroxide–graphene oxide composites, Chem. Commun. 48 (2012) 11416–11418.

[39] A. Primo, I. Esteve-Adell, S.N. Coman, N. Candu, V.I. Parvulescu, H. Garcia, One-step pyrolysis preparation of 1.1. 1 oriented gold nanoplatelets supported on graphene and six orders of magnitude enhancement of the resulting catalytic activity, Angew. Chem. 128 (2016) 617–622.

[40] A. Primo, E. Sánchez, J.M. Delgado, H. García, High-yield production of N-doped graphitic platelets by aqueous exfoliation of pyrolyzed chitosan, Carbon 68 (2014) 777–783.

[41] W. Wang, Z. Mao, Y. Ren, F. Meng, X. Shi, B. Zhao, Operando Raman spectroscopic evidence of electron–phonon interactions in NiO/TiO 2 pn junction photodetectors, Chem. Commun. 57 (2021) 12333–12336.

[42] K. Raj, B. Viswanathan, Synthesis of nickel nanoparticles with fcc and hcp crystal structures, Indian J. Chem. Sect. A 50 (2011) 176–179.

[43] W. Choi, J.-W. Lee, Graphene: Synthesis and Applications, CRC press, 2011.

[44] L. He, F. Weniger, H. Neumann, M. Beller, Synthesis, characterization, and application of metal nanoparticles supported on nitrogen-doped carbon: catalysis beyond electrochemistry, Angew. Chem. Int. Ed. 55 (2016) 12582–12594.

[45] B. Jurca, L. Peng, A. Primo, A. Gordillo, V.I. Parvulescu, H. García, Co–Fe nanoparticles wrapped on N-doped graphitic carbons as highly selective CO2 methanation catalysts, ACS Appl. Mater. Interfaces 13 (2021) 36976–36981.

[46] L. Peng, B. Jurca, A. Primo, A. Gordillo, V.I. Parvulescu, H. García, Co–Fe clusters supported on N-doped graphitic carbon as highly selective catalysts for reverse water gas shift reaction, ACS Sustain. Chem. Eng. 9 (2021) 9264–9272.

[47] S. Mao, C. Wang, Y. Wang, The chemical nature of N doping on N doped carbon supported noble metal catalysts, J. Catal. 375 (2019) 456–465.

[48] A. Pulido, M. Boronat, A. Corma, Theoretical investigation of gold clusters supported on graphene sheets, New J. Chem. 35 (2011) 2153–2161.

[49] X. Zhou, W. Chu, W. Sun, Y. Zhou, Y. Xue, Enhanced interaction of nickel clusters with pyridinic-N (B) doped graphene using DFT simulation, Comput. Theoret. Chem. 1120 (2017) 8–16.

[50] A.P. Grosvenor, M.C. Biesinger, R.S.C. Smart, N.S. McIntyre, New interpretations of XPS spectra of nickel metal and oxides, Surf. Sci. 600 (2006) 1771–1779.

[51] Thermofischer, Nickel X-ray photoelectron spectra, nickel electron configuration, and other elemental information, 2023.

[52] X. Li, H. Cheng, G. Liang, L. He, W. Lin, Y. Yu, F. Zhao, Effect of phosphine doping and the surface metal state of Ni on the catalytic performance of Ni/Al2O3 catalyst, Catalysts 5 (2015) 759–773.

[53] N. Rodriguez, P. Anderson, A. Wootsch, U. Wild, R. Schlögl, Z. Paál, XPS, EM, and catalytic studies of the accumulation of carbon on Pt black, J. Catal. 197 (2001) 365–377.

[54] J. Liu, M. Jiao, L. Lu, H.M. Barkholtz, Y. Li, Y. Wang, L. Jiang, Z. Wu, D.-J. Liu, L. Zhuang, C. Ma, J. Zeng, B. Zhang, D. Su, P. Song, W. Xing, W. Xu, Y. Wang, Z. Jiang, G. Sun, High performance platinum single atom electrocatalyst for oxygen reduction reaction, Nat. Commun. 8 (2017) 15938.

[55] N.J. Shevchik, D. Bloch, XPS d bands and core levels of Pt-Ni alloys, J. Phys. F Metal Phys. 7 (1977) 543–550.

[56] D. Mateo, I. Esteve-Adell, J. Albero, J.F.S. Royo, A. Primo, H. Garcia, 111 oriented gold nanoplatelets on multilayer graphene as visible light photocatalyst for overall water splitting, Nat. Commun. 7 (2016) 1–8.

[57] X. Ye, Y. An, G. Xu, Kinetics of 9-ethylcarbazole hydrogenation over Raney-Ni catalyst for hydrogen storage, J. Alloys Compd. 509 (2011) 152–156.

[58] E. Tiburcio, R. Greco, M. Mon, J. Ballesteros-Soberanas, J. Ferrando-Soria, M. López-Haro, J.C. Hernández-Garrido, J. Oliver-Meseguer, C. Marini, M. Boronat, D. Armentano, A. Leyva-Pérez, E. Pardo, Soluble/MOF-supported palladium single atoms catalyze the ligand-, additive-, and solvent-free aerobic oxidation of benzyl alcohols to benzoic acids, J. Am. Chem. Soc. 143 (2021) 2581–2592.

[59] S.J. Teichner, Recent studies in hydrogen and oxygen spillover and their impact on catalysis, Appl. Catal. 62 (1990) 1–10.